Electronic Supporting Information

NOM-assisted, Amyloid-enriched, Hierarchical Self-assembled Nanostructures of Maghemite Nanoparticles and their Plastic Deformation: Role of Magnetic Fields, Pb^{2+}, and Biomolecular Conformations

Qijing Xu[a], Hui Dong[a], Zhenquan Wang[a], Bo Su[a], Nihar R. Pradhan[b, c]

Di Zhang[a], Saikat Ghosh[a]*, Bo Pan[a], Baoshan Xing[d]*

[a]Kunming University of Science and Technology, Kunming, China 650500

[b]Jackson State University, Department of Chemistry, Physics and Atmospheric Science,1400 John R. Lynch Street, Jackson, Mississippi 39217, United States

[c]National High Magnetic Field Laboratory, 1800 E. Paul Dirac Drive,

Tallahassee, FL, 32310, Unites States

[d]Stockbridge School of Agriculture, University of Massachusetts, Amherst, Massachusetts 01003, United States

*Corresponding Authors; E-mail: saikatgh.1970@gmail.com (Saikat Ghosh)

Table S1. Elemental analysis data

	C (%)	N (%)	H (%)	S (%)
G-FeNP	0.399	0	0.381	0.212
B1-GFeNP	3.999	0.896	0.549	1.123
B1-GFeNP + HA	7.52	1.19	0.786	1.232
B2-GFeNP	10.9	2.25	1.36	1.286

Magnetic Properties

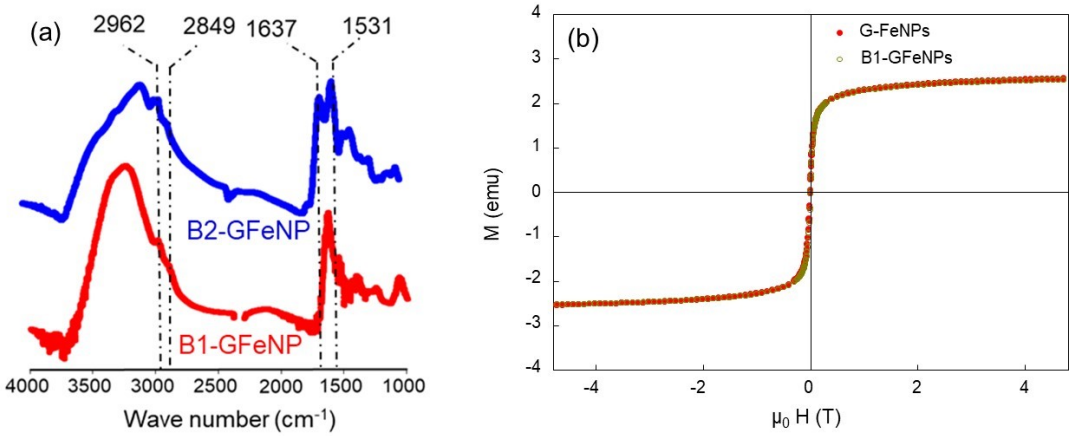

Figure S1. (a) DRIFT spectra of B2-GFeNPs and B1-GFeNPs exhibiting surface functionalization of maghemite NPs. These spectra are plotted after subtracting the complex conjugate spectra from the bare maghemite. (b) The BSA adsorption on maghemite NPs surface caused a minimal loss in magnetic moment.

A weighted amount of the powdered samples was poured into gelatin capsules, which were then inserted into a DC-SQUID magnetometer equipped with a superconducting Josephson junction cooled in liquid helium. The blocking temperature (T_B) of the samples was determined from the M-T data obtained by cooling the samples from 300 K to ≈ 0 K in the absence of any applied

magnetic field to obtain the zero-field cooled (ZFC) data followed by heating the samples from ≈ 0 K to 300 K in a magnetic field. The efficiency of the surface-modified magnetic NPs in remediation of contaminated water resources is incumbent upon their colloidal dispersibility and interaction potentials with the contaminant heavy metal ions, especially surface modifiers. The significantly higher moment of the magnetic core can induce strong destabilizing magnetic dipolar force and subsequent loss in effective surface area. Bare G-FeNPs showed a saturation magnetization (M_s) of 60 emu/g from the M-H data measured at both 1.8 K and 295 K. However, magnetic hysteresis was detected only at 1.8 K reflecting thermal fluctuations induced loss of magnetic moments.

Thermal gravimetric analysis (TGA) and Differential Thermal Gravimetric (DTG)

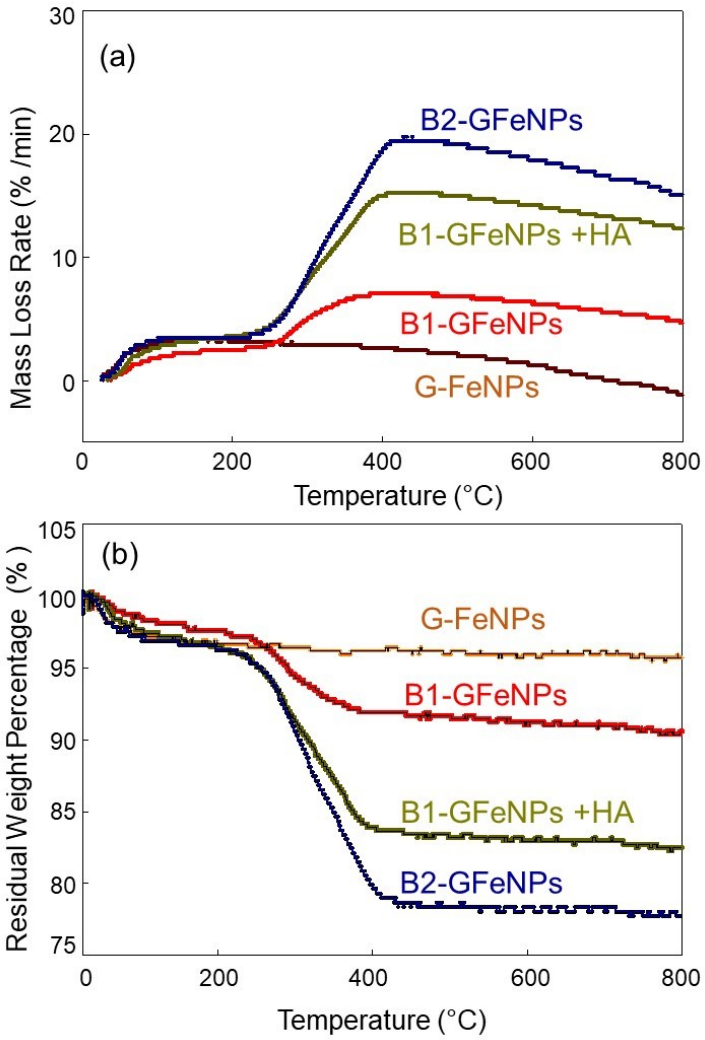

Figure S2. TGA and DTG data of G-FeNPs, B1-GFeNPs, intermediate, and B2-GFeNPs.

The heat loss of the bare G-FeNP, B1-GFeNP, and B2-GFeNP was determined using a differential thermogravimetric Analyzer (TGA, DTG-60H, Japan). Approximately 5 mg of the samples obtained after magnetic separation and centrifugation followed by freeze-drying were then heated from 25ºC to 800°C in a TGA analyzer with 10 °C/minute ramp speed in the air atmosphere. The mass-loss rate (%) and the residual weight percentages were plotted against temperature.

Determination of surface charge

Brookhaven Zeta PALs (Newhaven, U.S.A.) instrument employs a 633 nm He–Ne laser and collects back-scattered data at 173°. Electrophoretic mobility (μ) was measured by inserting the suspensions (1.6 mL of 20 mg. L^{-1}) in plastic cuvettes followed by measurements using laser Doppler velocimetry and phase analysis light scattering technique in a.

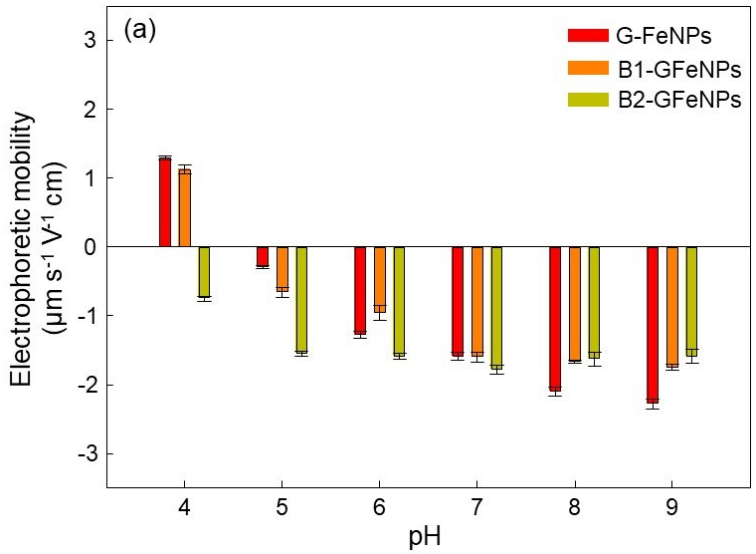

Figure S3. EPM data of G-FeNPs, B1-GFeNPs and B2-GFeNPs within pH 4 to pH 9 range.

X-ray Diffraction and Transmission electron microscopy (TEM)

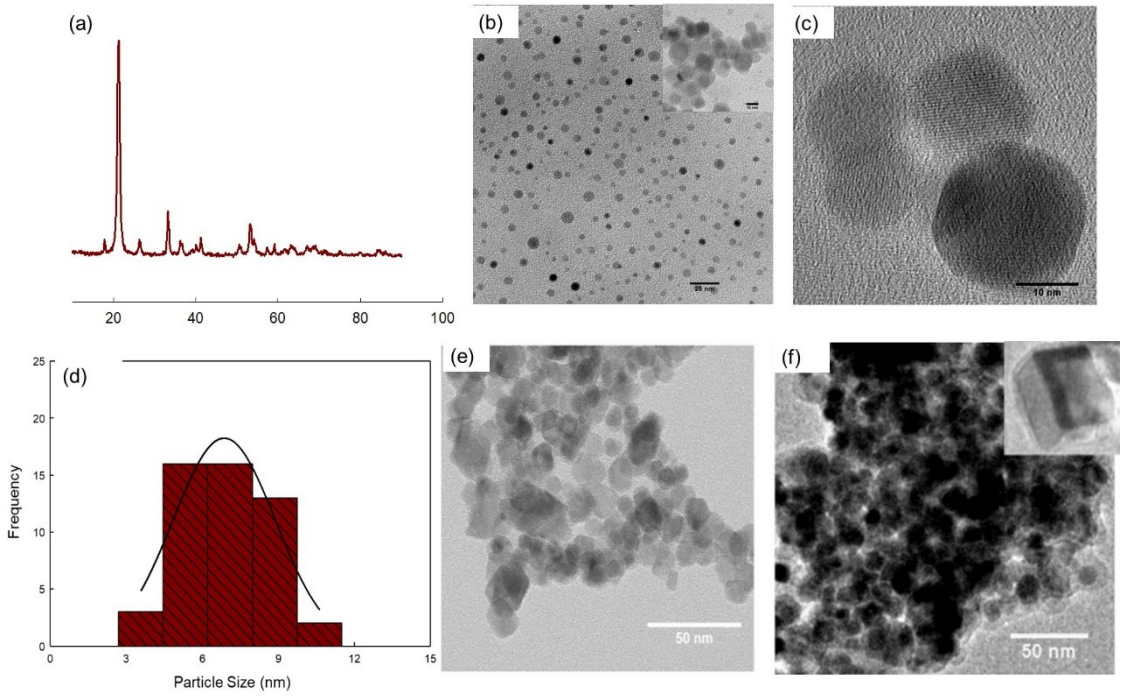

Figure S4. (a) XRD data of G-FeNPs. (b) TEM images of B1-GFeNPs at pH 4 showed both the presence of dispersed and aggregated particles due to reduced sorption of BSA and lower steric stabilization. (c) The TEM image of B1-GFeNPs showed that it had a slightly cuboid-like geometry. (d) The particles size distribution data of B1-GFeNPs. (e) Increasing the suspension pH of B1-GFeNPs from 4 to 7 also showed the formation of aggregates revealing magnetic dipolar force-mediated aggregation. (f) The self-assembly behavior of B2-GFeNPs with FCC-like arrangement and eventual growth of colloidal crystal (inset).

Diffuse Reflectance Fourier transformed infrared spectroscopy (DRIFT) and Raman spectroscopy

The colloidal suspensions of both B1-GFeNP and B2-GFeNP were centrifuged in a high-speed refrigerated centrifuge (GL-21M, Yingtai Instrument, China) at 20000 rpm for15 minutes followed by freeze-drying. The freeze-dried samples were then mixed with the grounded KBr by maintaining a 1:100 (w/w) ratio. The obtained spectra were then subtracted from the pure G-FeNP spectrum. Raman spectra of the samples were collected with a Horiba Raman X-ploRA Plus

equipped with a 532 nm laser with 50% filter, 600 grating/mm, and 100 µm slit size. 20 mg/L B2-GFeNP suspension in the presence and absence of 100 mg/L Pb^{2+} were allowed to dry on glass slides followed by scanning within 100-2000 cm^{-1} region.

Theory of ^1H spin relaxation

In a static magnetic field, proton magnetic moments of water precess at the Larmor frequency, which is proportional to the local magnetic field. The local fluctuations of the external magnetic field due to magnetic moments of the NPs, and the diffusivity of the proton determine the rate of proton spin dephasing. The mathematical expression for the local magnetic inhomogeneity evolved from the cluster size variation in a uniform precessing magnetic field affecting the rate of relaxation is:

$$B\ (r,\ \theta) = \frac{\mu_0 m}{4\pi}\left[\frac{3\ Cos^{\ 2}(\theta) - 1}{r^3}\right] \quad \text{.....(1)}$$

Where *B* is the external magnetic field, *r* is the NPs radius, *m* is the NPs magnetic moment pinned along the Z-direction. Since the external "Z"-directed magnetic field is sufficiently strong to overcome mutual interactions between NPs, *r* is the position of ^1H nuclei from the center of the magnetic field, θ is the angle with the Z-axis, and μ_0 is the permeability of the free space. The transverse relaxation (R_2=1/T_2) is defined as the decay of coherently precessing ^1H spins. Hahn (2011) proposed that the inhomogeneities of the external magnetic field that dominates the relaxation process can be overcome by nuclear induction applying radio frequency (rf) pulses.[1] Moreover, the pH-dependent conformational alteration of the protein-rich complex biomolecules due to their solvation in an aqueous medium contributes to the exchange of neighboring water molecules may also contribute to ^1H spin relaxation. Teflon tape was used to seal the tube to minimize solvent loss and maintenance of particle-solvent ratio. In this regard, a Carr–Purcell–

Meiboom–Gill (CPMG) pulse sequence using 200-600 echo cycles with echo spacing (τ = 0.5 ms) and with 90º and 180º pulse sequence of 8 μS and 17 μS durations respectively. The rate of change of T_2 as a function of waiting time (t_w) was measured at time t = 0 to t =1000s after 30-second intervals with nearly 30 data points for each sample. The R_2 data was then fitted with a biexponential decay function:

$$R_2(t) = R_2(\infty) + Ae^{-\Lambda_A t} + Be^{-\Lambda_B t} \quad \ldots\ldots\ldots\ldots (2)$$

Topological Transformation and Helfrich bending

According to Helfrich's model based on Gibbs-interfacial energy, the elastic modulus of membrane bending is proportional to the bending moment in X-Y plane and Gaussian curvature of complex layers. Theoretically, the total curvature energy (F_B) of aggregates follows the equation:

$$F_B = \oint dA \left[\frac{1}{2}\kappa\left(\frac{1}{R^1} + \frac{1}{R_2} - \frac{2}{R_0}\right)^2 + \bar{\kappa}\left(\frac{1}{R_1 R_2}\right)\right] \quad \ldots\ldots\ldots\ldots..(3)$$

R_1 and R_2 are the principal radii of curvature with mean curvature $\left(H = \frac{1}{2\left(\frac{1}{R_1} + \frac{1}{R_2}\right)}\right)$, R_0 is the spontaneous radius of curvature, and κ *and* $\bar{\kappa}$ are the mean and the Gaussian curvature elastic constants, and A is the area of the thin-film forming the object. The first term in equation (1) refers to the role of mean curvature on the aggregate size of the same topology. However, the second term $K = 1/R_1R_2$ determines the contribution of the Gaussian curvature. Aggregates with larger dimension, with negligible difference between the mean and spontaneous curvature R_0 and H, the second term K determined the aggregate topology or Gaussian curvature of the aggregates that control the bending moment:

$$F_B = \bar{\kappa}\oint KdA\,, \qquad where \oint KdA = 4\pi\,(1-g) \quad \text{.....(4)}$$

g = genus of the aggregate which is 0 for spherical clusters.

In situ AFM and TEM images of magnetic field-assisted assembly of B2-GFeNPs

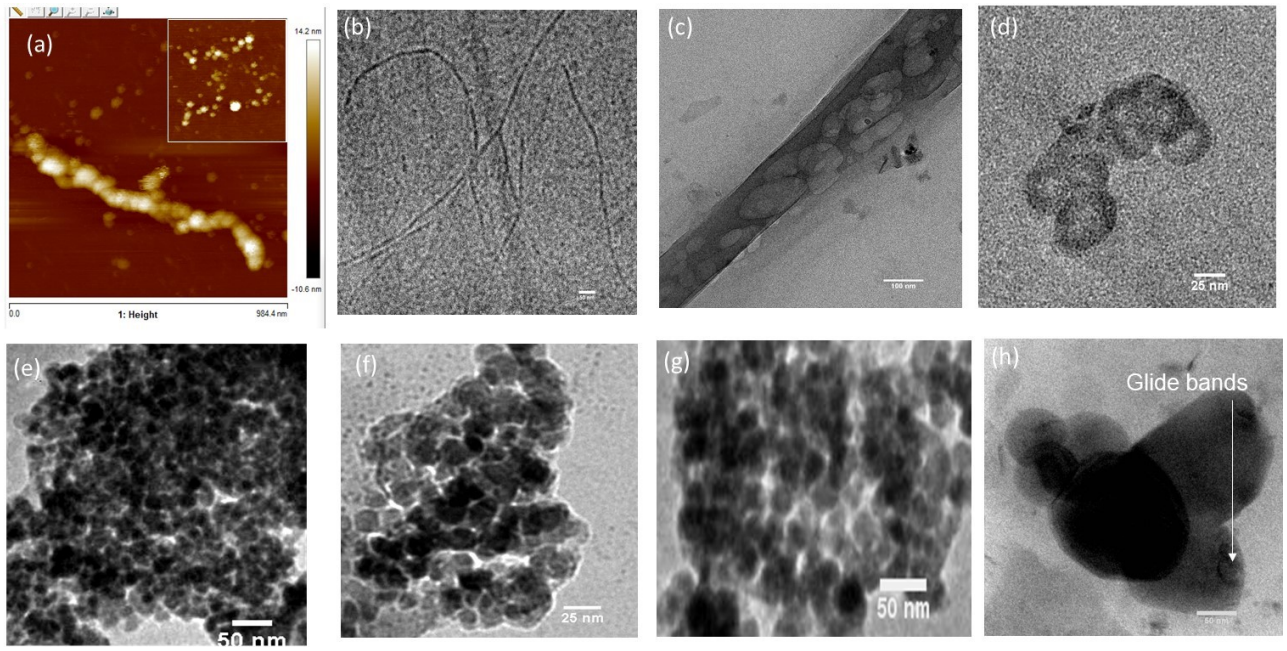

Figure S5. Magnetic field-assisted assembly of B2-GFeNPs with (a) high Fe/C ratio also showed screw-dislocation mediated growth of tubular growth. B2-gFeNPs with low Fe/C showed (b) amyloids, and the growth of (c) nanotubular geometry. (d) The spheroidal structures which were stacked together in the presence of an external magnetic field possibly contributed to tubular growth. (e-g) TEM images of B2-GFeNPs at pH 4 showed chirality-assisted assembly of nanoclusters. (g-h) Screw dislocation-driven growth of colloid clusters with the piling up of dislocations in the larger cluster with indicated glide bands.

The Role of elastic stress on dislocation motion and particle arrangement at pH 4 and pH 7 and in the presence of Pb^{2+}

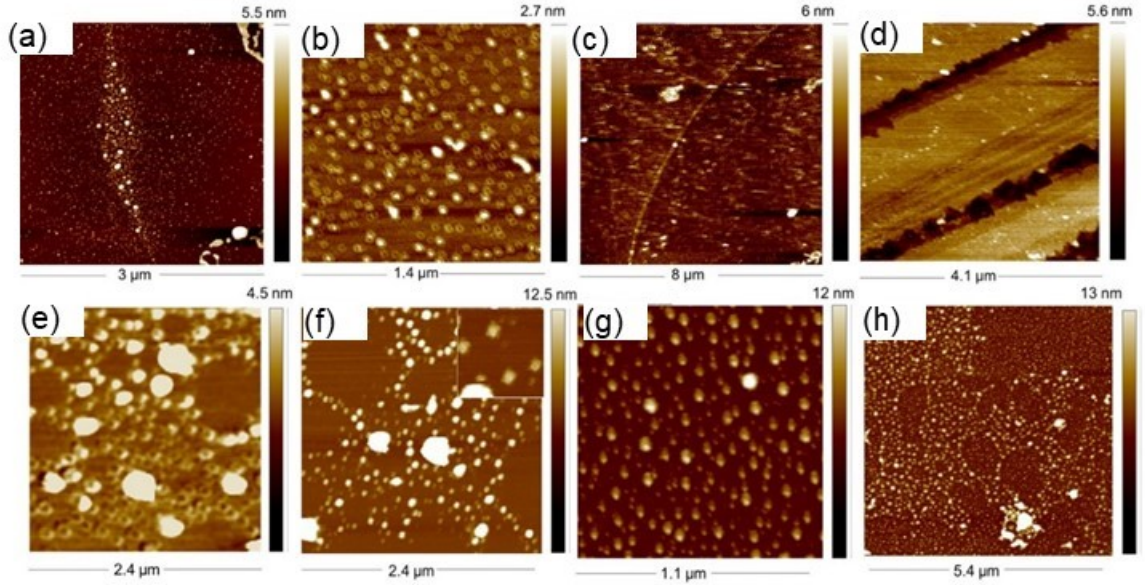

Figure S6. (a-d) *In situ* AFM images of B2-GFeNP in the presence of Pb^{2+} at pH 4 shows (a) Eshelby-twisted growth of aggregates (b) Orowan's mechanism and the presence of dislocation loop around hard clusters (c) Screw dislocation-driven growth of wire and (d) cracking of aggregates under strong elastic strain. Time-lapse *in situ* AFM images of B2-GFeNP at pH 7 in the presence of Pb^{2+}shows (e) cutting of the precipitate (f) nested loop arrangement of clusters (g-h) dislocation pile up and layered growth of B2-GFeNP at 7.

Young's modulus measurement

A silicon nitride (Si_3N_4) cantilever (BL-AC40TS-C2, Japan) with an average resonance frequency of 25 kHz in water and a spring constant of 0.09 N/m with a probe radius of 8 nm was used to obtain the force data. Before force measurements B2-GFeNPs suspensions mainatianed at pH 4 and pH 7 was equilibrated with freshly cleaved mica surface followed by addition of Pb^{2+} solution. The force data were fitted with Derjaguin-Muller-Toporov (DMT) model using Igor-pro software with a linearized DMT model. Young modulus equation can be calculated as follows:

$$F_{sphere} - F_{adh} = \frac{4}{3} \cdot \frac{E}{1 - v^2} \sqrt{R} \delta^{3/2} \quad \ldots\ldots\ldots \quad (5)$$

$$E = \frac{3}{4}\left(\frac{\Delta\left(F_{sphere} - F_{adh}\right)^{\frac{2}{3}}}{\Delta\delta}\right)^{\frac{3}{2}}\frac{1-\nu^2}{\sqrt{R}} \qquad \text{…….(6)}$$

Where F_{sphere} is the applied force, R is the indenter radius, δ is the indentation depth, E is the Young modulus, v is the Poisson ratio, F_{adh} is the adhesion force.

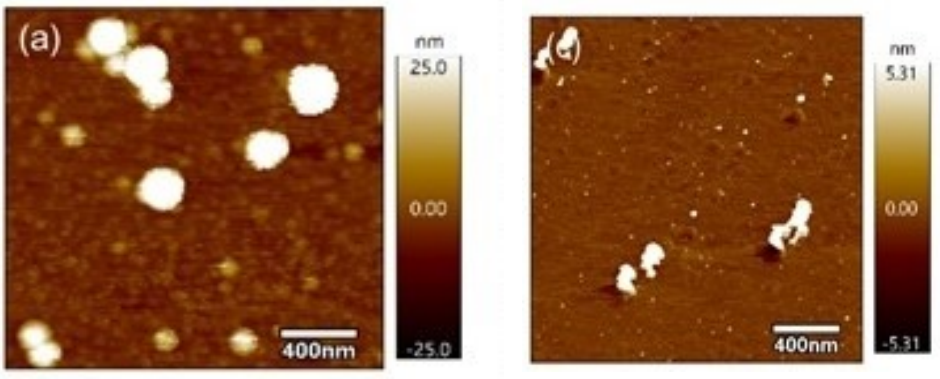

Figure S7. AFM height images of B2-GFeNP in the presence of 50 µg/L Pb^{2+} (a) at pH 4 and at pH 7. These images were obtained during Young's

moduli measurements.

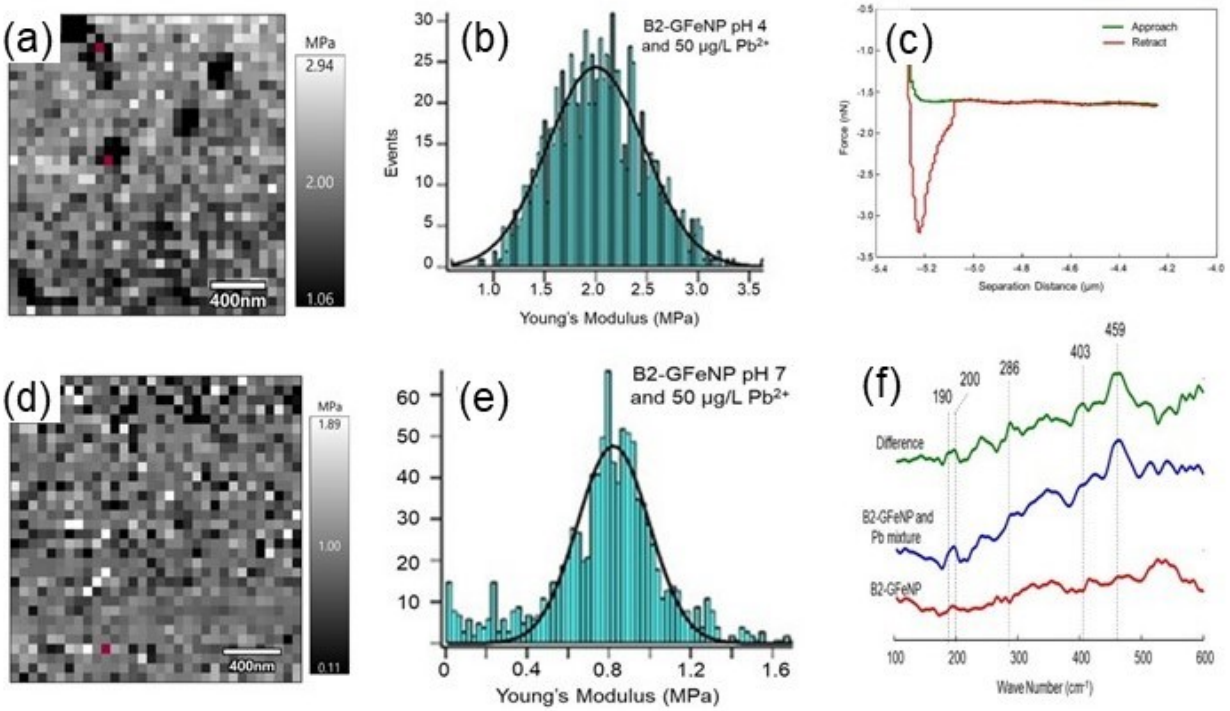

Figure S8. *In situ* AFM adhesion force maps of B2-GFeNPs in the presence of 50 µg/L Pb^{2+} with a Gaussian distribution of Young's modulus (a-b) 2.3 M Pa at pH 4 and (c) Typical adhesion force curve of B2-GFeNPs in the presence of 50 µg/L Pb^{2+} at pH 4. The retract curve shows strong probe-substrate adhesion. (d-e) *In situ* AFM adhesion force maps of B2-GFeNPs in the presence of 50 µg/L Pb^{2+} and the Gaussian distribution of the Young's modulus at pH 7 (~ 0.8 M Pa). (f) Raman spectra of 20 mg/L B2-GFeNPs, mixture of B2-GFeNPs with 100 mg/L Pb^{2+}, and the difference spectra exhibiting vibrations associated with *in situ* nucleation of nanocrystalline PbS at pH 4.

E_h-pH diagram of Pb

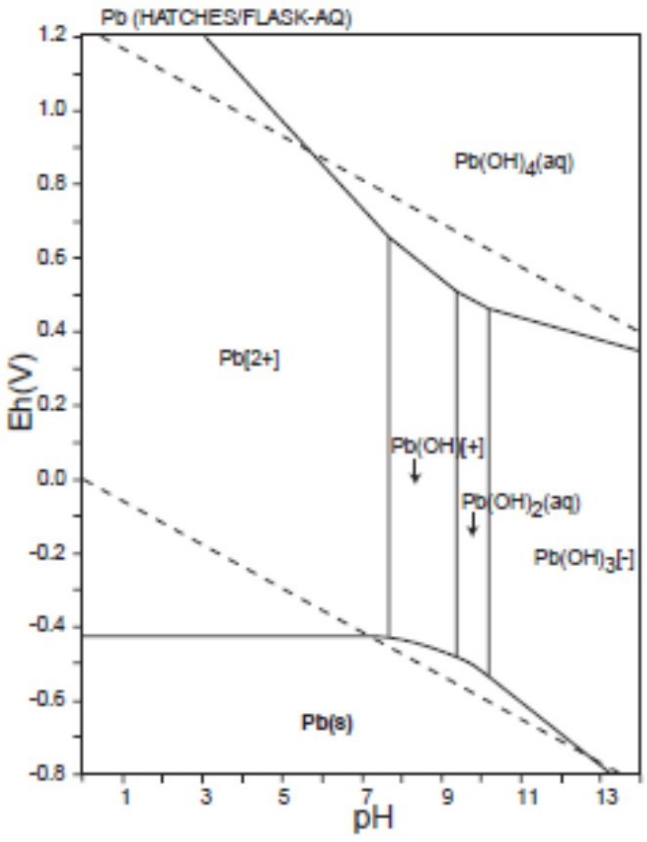

Figure S9. E_h-pH diagram of Pb^{2+} (obtained from Japan Geophysical Society)

Young's moduli and elasticity maps, and in situ growth of PbS: Role of pH and Pb^{2+} speciation

Determination of Young's moduli and elasticity maps of 10 mg/L B2-GFeNPs suspensions with 50 ppb Pb^{2+} on the mica surface both at pH 4 and pH 7 further corroborated Young's moduli of 1.97 MPa and 0.865 MPa, respectively (Figures S7 and S8). The typical tip-sample adhesion force data obtained at pH 4 are shown (Figure S8c). Earlier studies have also shown extremely stable binding of Pb^{2+} with low molecular weight proteins with an apparent dissociation constant (K_d) for Pb^{2+} of 10^{-8} M.[4] Chen et al. reported the selective binding of a novel Pb^{2+}-regulatory protein in *Ralstonia metallidurans* CH34 to a fluorescent reporter that exhibits high selectivity and sensitivity.[2] Considering the abundance of S-containing functional moieties in B2-GFeNP seen from the elemental composition and STM mapping (Please see Table S1, and Figure 5 in the main text), we further investigated whether the specific binding of Pb^{2+} with B2-GFeNP can lead to mineralization of PbS. BSA contains 34 oxidized (disulfide-linked) cysteine residues and one reduced cysteine residue and has shown a strong affinity toward Ag NP dissolution.[3] Raman scattering of the 20 mg/L B2-GFeNP and 100 mg/L Pb^{2+} mixture and subtraction of the Raman spectra from B2-GFeNPs at pH 4 revealed signatures of *in situ* PbS nanocrystal formation (Figure S8f). The Raman shift usually corresponds to longitudinal optical (LO) phonons, transverse optical phonons (TO), and surface phonons (SP). However, Raman SP vibrations in PbS (*Fm3m* space group) are nullified due to symmetry restrictions; hence, except for LO, the TO and SP vibrations

were not observable.[4] Baranov et al. (2010) pointed out that Raman scattering yields only weak second- and higher-order Raman lines from phonons at the critical points of the Brillouin zone.[5] The Raman peaks observed at 200 cm^{-1}, 286 cm^{-1}, and 459 cm^{-1} represent the 1 LO phonon and 2 LO phonon modes. The peaks observed at 190 cm^{-1} possibly represent the SP vibration mode.[6] Portillo-Moreno et al. pointed out that the intensity of the SP vibration band at ~192 cm^{-1} increased with decreasing particle size.[4] Ge et al. showed that the 190 cm^{-1} Raman peak is specific to very small nanocrystals and nanowires.[7] Therefore, it is likely that the helicity-driven assembly of maghemite NPs in B2-GFeNPs provides the necessary scaffold for co-crystallization of PbS via screw dislocation-driven Eshelby-twisted growth. Therefore, this study provides a method of entrapping heavy metal ions from solution and a potential application in the scaffold-controlled synthesis of low bandgap PbS for energy harvesting.

TEM images of B2-GFeNPs in the presence of Pb^{2+} at pH 4

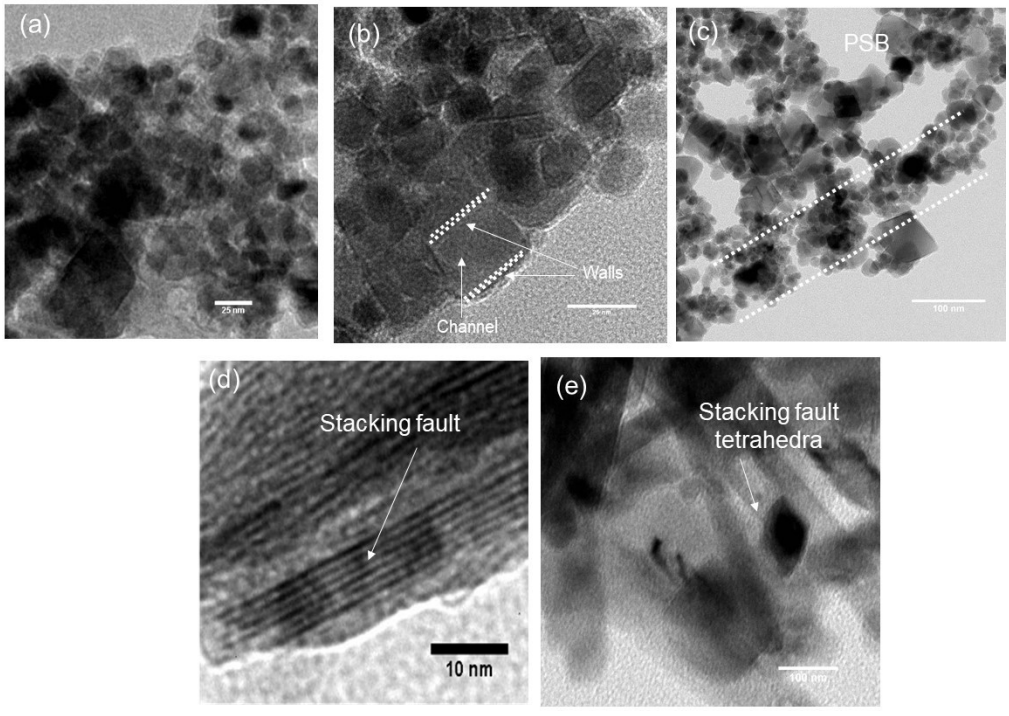

Figure S10. Pb^{2+}-induced (a) elastic strain on the growth geometry of B2-GFeNPs. (b-c) Formation of PSBs. Dislocation annihilation due to mutual interactions led to PSBs formation. (d) Elastic strain due to nucleation of Pb^{2+} produced stacking fault and (e) stacking fault tetrahedra with enrichment of defects along with the formation of tubular grains.

TEM images of B2-GFeNPs in the presence of Pb^{2+} at pH 7

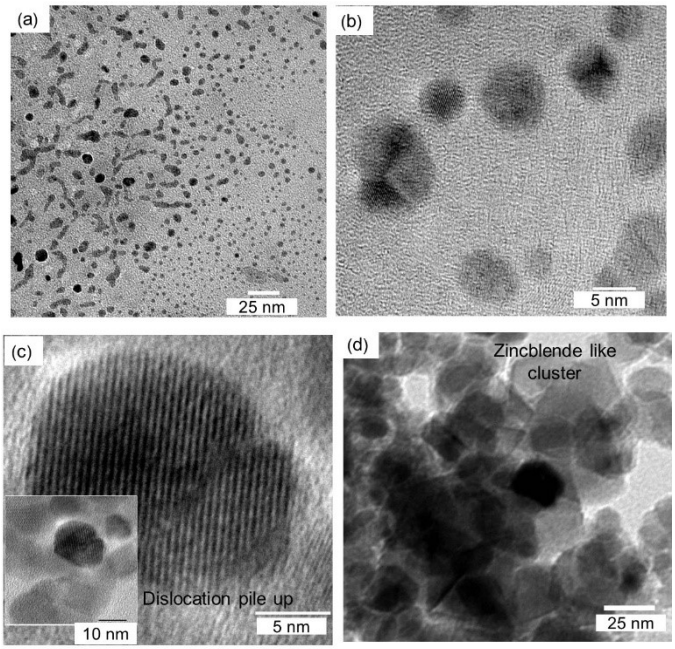

Figure S11. Pb^{2+}-induced elastic strain on the growth geometry of B2-GFeNPs at pH 7 elicited the growth of zincblende-like platelet-like nano-scale colloidal crystals.

References

1. H. W. de Haan, Mechanisms of proton spin dephasing in a system of magnetic particles. *Magnetic Resonance in Medicine*, 2011, 66, 1748–1758.

2. B. A. Fowler, Roles of lead-binding proteins in mediating lead bioavailability, *Environ. Health Perspect.*, 1998, 106, 1585-1587.

3. P. Chen, B. Greenberg, S. Taghavi, C. Romano, D. van der Lelie and C. He, An exceptionally selective lead(ii)-regulatory protein from Ralstonia Metallidurans: development of a fluorescent lead (ii) probe, *Angew. Chem. Int. Ed.*, 2005, 44, 2715 –2719.

4. A-K. Ostermeyer, C. K. Mumuper, L. Semprini and T. Radniecki.. Influence of bovine serum albumin and alginate on silver nanoparticle dissolution and toxicity to *Nitrosomonas Europaea*. *Environ. Sci. Technol.*, 2013, 47 (24), 14403–14410.

5. O. Portillo-Moreno, R. Guti´errez-P´ereza, M. Ch´avez Portillo, M. N. M´arquez Specia, G. Hern´andez-T´ellez, M. Lazcano Hern´andez, A. Moreno Rodr´ıguez, R. Palomino-Merino and E. Rubio Rosas. Growth of doped PbS:Co^{2+} nanocrystals by chemical bath, *Rev. Mex. Fis.*, 2016, 62, 456–460.

6. V. Baranov, K. V. Bogdanov, E. V. Ushakova, S. A. Cherevkov, A. V. Fedorov and S. Tscharntke, Comparative analysis of Raman spectra of PbS macro and nanocrystals, *Optics and Spectroscopy*, 2010, 109 (2), 268–271.

7. J-P. Ge, J. Wang, H-X. Zhang, X. Wang, Q. Peng and Y-D, Li, Orthogonal PbS nanowire arrays and networks and their Raman scattering behavior, *Chem. Eur. J.*, 2005, 11, 1889 – 1894.